Proceedings World Geothermal Congress 2015
Melbourne, Australia, 19-25 April 2015

Diffuse Degassing Measurements in Geothermal Exploration of Fault Controlled Systems

Egbert Jolie[1], Matthias Klinkmueller[2], Inga Moeck[3]

[1]Telegrafenberg, 14473 Potsdam, Germany

[2]Aker Wirth, Koelner Strasse 71-73, 41812 Erkelenz, Germany

[3]University of Alberta, Edmonton, Alberta, Canada

jolie@gfz-potsdam.de

Keywords: Brady's, Basin-and-Range Province, diffuse degassing, exploration, fault controlled systems

ABSTRACT

An improvement in surface exploration of fracture controlled geothermal systems shall be achieved by a combined approach of different techniques for diffuse degassing measurements. Gas emissions provide valuable insights into the reservoir characteristics and allow the detection and assessment of permeable fracture zones, which are the preferential targets for geothermal production wells. Areas with high gas emissions can be used as an indicator of major upflow zones from the reservoir through deep reaching, permeable fault zones. The study summarizes two in-situ techniques for the assessment of diffuse degassing processes in geothermal fields from which relative structural permeability has been deduced. This includes spectroscopic measurements of alpha radiation for the determination of the gaseous decay products ^{222}Rn (radon) and ^{220}Rn (thoron), as well as CO_2 and H_2S measurements by the accumulation chamber method. Both techniques are combined with a method for the determination of electromagnetic gamma radiation. Diffuse degassing measurements are strongly considered to be a successful detection and assessment tool for permeable structural elements. This approach is applied to the Brady's geothermal system in the Basin-and-Range Province, USA.

1. INTRODUCTION

Diffuse degassing measurements have already been applied for various purposes worldwide, such as volcanic hazard analysis, environmental monitoring and others (Hernández et al., 2001; Cardellini et al., 2003; Pérez et al., 2004; Fridriksson et al., 2006; Chiodini et al., 2010). Besides these well-established applications, gas measurements hold the potential to provide a useful tool for the identification of permeable zones in fracture-controlled geothermal reservoirs (Giammanco et al., 1998; Padrón et al., 2003). The aim of this study is to show that extensional tectonics in the Basin-and-Range Province (Brady's geothermal system) facilitates gas migration from deep sources to the surface due to abundant deep-reaching fault systems (Fig. 1). Herein, exemplary results of two exploration techniques for measurements of invisible diffuse degassing processes are presented, which are not yet commonly and systematically applied in geothermal exploration campaigns (Jolie et al., 2012b, 2014b).

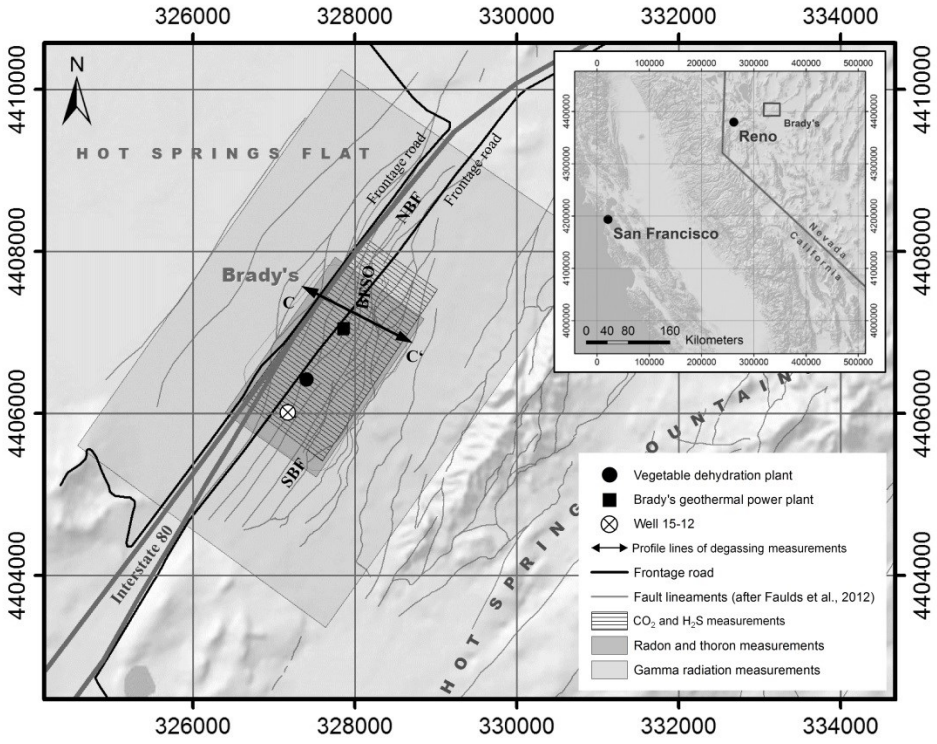

Figure 1: Local sketch map of the Brady's geothermal system illustrating the schematic boundaries of the surveyed area for the applied methods (modified from Jolie et al., 2014b). SBF: Southern Brady's fault; NBF: Northern Brady's fault; BFSO: Brady's fault step over; Coordinate System: NAD 1983 UTM Zone 11N.

2. METHODS

2.1 CO_2 measurements

The measurements of diffuse CO_2 emission rates were performed according to the accumulation chamber method (Parkinson, 1981). This method allows a real time analysis without any necessary ground installation of sampling devices (Jolie et al., 2012b, 2014b). A portable flux meter (West Systems) has been used for the combined analyses of CO_2 and H_2S (Fig. 2A). The instrument is equipped with a LICOR LI-820 carbon dioxide analyzer (West Systems, 2002). The integrated software PalmFlux supported the measurement by quantifying the emission rates of CO_2 by determining the slope of the increasing concentration in the accumulation chamber over time (Fig. 2B). A linear regression line with a high regression quality factor ErrQ > 0.9 was fitted onto the exponential curve by manual selection of a regression interval. In general, the best fit can be obtained immediately after starting the measurement when the gas begins to accumulate inside the chamber. Due to the barometric pressure and air temperature dependence both parameters have been recorded at each sampling site for data processing and were considered for the selection of the accumulation chamber factor, which was required for data conversion from ppm/s to g/m^2/d (West Systems, 2002). A regular grid of sampling sites over the entire study area was realized. In the vicinity of geothermal surface manifestations further measurements were added for a better delineation of the degassing anomalies.

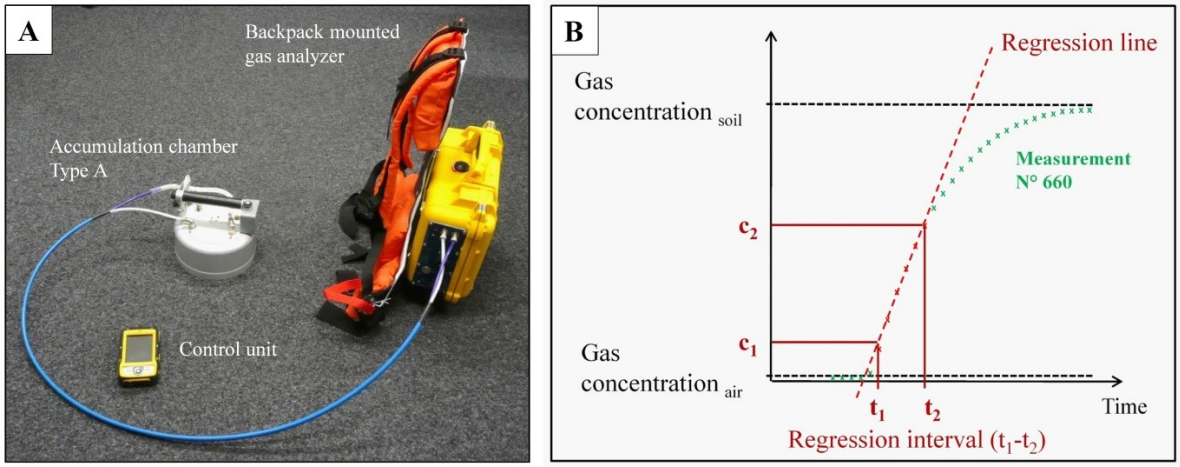

Figure 2: (A) Device for CO_2 and H_2S measurements, which consists of the accumulation chamber (type A), the gas analyzer and the control unit (PDA), operating the measurement via Bluetooth connection (from Jolie et al., 2014b). Recorded data can be stored in the PDA. (B) The diagram shows an example plot of measured gas concentration over time and represents the increase of gas concentration in the accumulation chamber (from Jolie et al., 2014b). A regression line between t_1-c_1 and t_2-c_2 (regression interval) has to be fit into the curve to provide the gas flux in ppm/s.

2.2 Alpha radiation

The radiometric measurement of radon and thoron activity concentration in soil gas was performed with two Sarad RTM 2200 monitors (Fig. 3A). The gaseous radon isotopes ^{222}Rn (radon) and ^{220}Rn (thoron) have been studied simultaneously (Fig. 3B). At each sampling site a metal probe was inserted approximately 1 m into the ground. The soil gas was pumped at a constant rate through a tube connected to the gas analyzer. Due to the half-life of ^{218}Po minimum measurement duration for each sampling site was 15 min (Fig. 4).

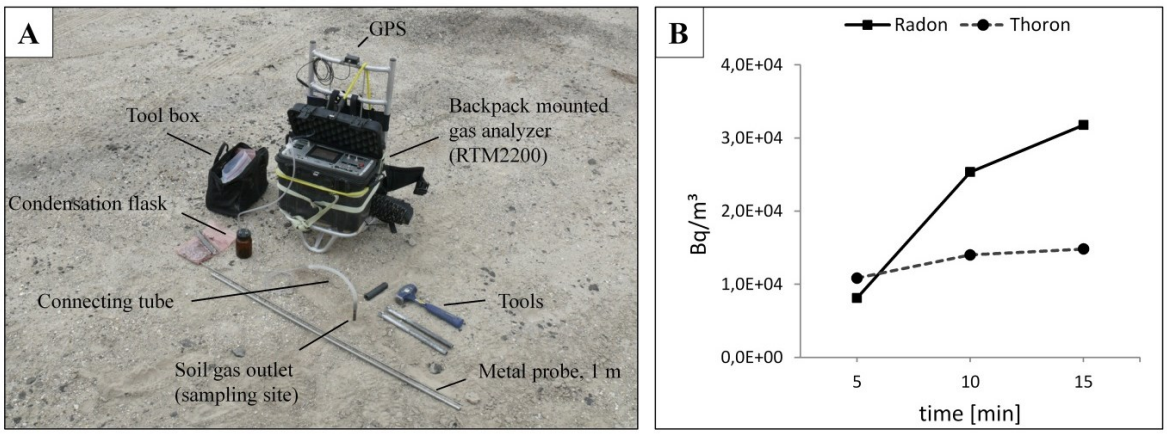

Figure 3: (A) Device for alpha-particle spectroscopic measurements of ^{222}Rn (radon) and ^{220}Rn (thoron) (from Jolie et al., 2014b). All readings, including GPS coordinates, have been stored in the RTM2200. (B) Two example graphs (radon and thoron) are plotted in the diagram over time (from Jolie et al., 2014b). Each graph shows the increase of activity for each nuclide. After 15 minutes the measurement was stopped and data were saved.

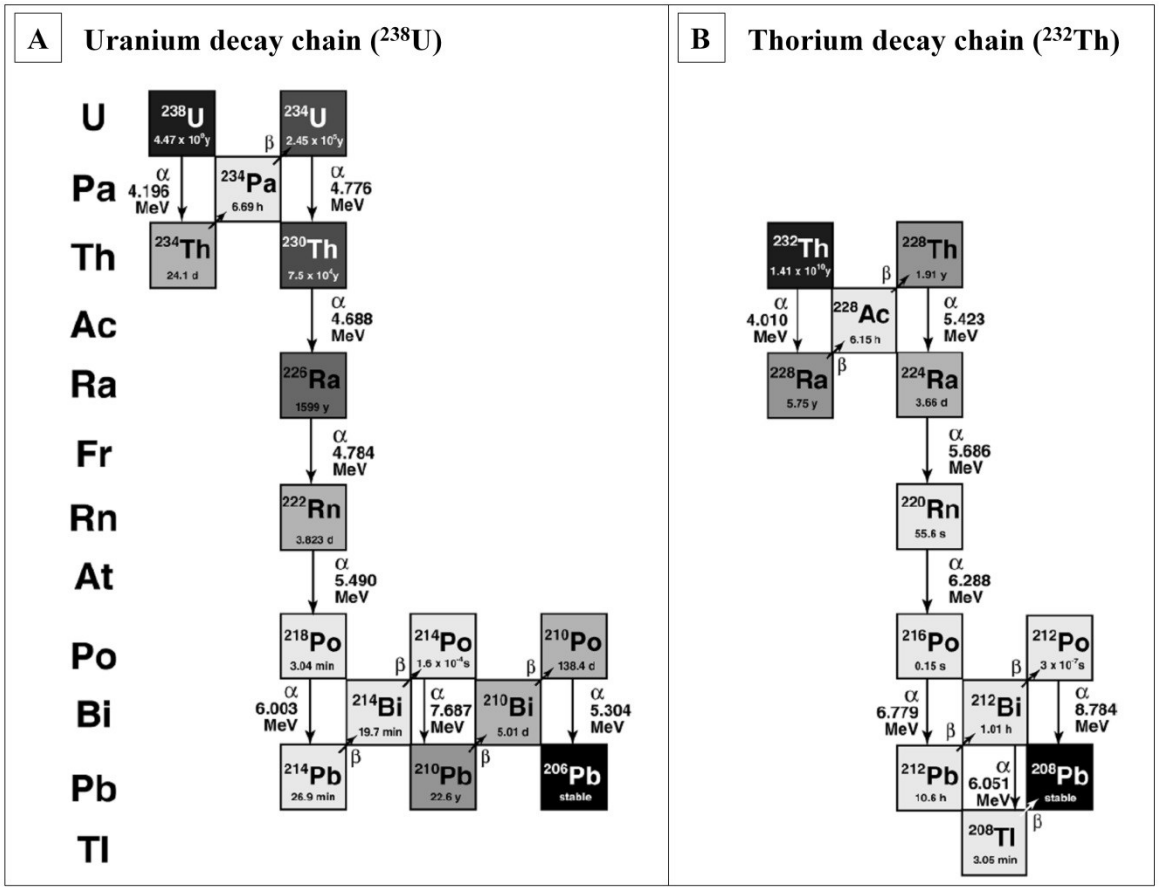

Figure 4: (A) ^{238}U decay chain and (B) ^{232}Th decay chain (modified after Bourdon et al., 2003). The fast mode measurement of radon determines the primary decay of ^{218}Po. The thoron measurement determines the primary decay of ^{216}Po.

3. RESULTS

Detailed data processing and analysis was carried out for a comprehensive understanding of the gas emissions at the Brady's geothermal field. Results have been related to the mapped fault pattern (Faulds and Garside, 2003; Faulds et al., 2012 and unpublished data) and the 3D structural-geological model (Jolie et al., 2012a, 2014a). The findings for all parameters show a broad distribution of signals. Strong variations of gas fluxes have been determined in particular along mapped fault zones, which reach into the geothermal reservoir as shown in the 3D structural-geological model of the Brady's field, but also in areas without obvious evidence of faulting or geothermal surface manifestations (Jolie et al., 2012a,b, 2014a,b). The detected degassing anomalies are used to infer relative structural permeabilities and might help to better delineate the potential reservoir at depth. In the following paragraphs results of two exemplary parameters (CO_2, ^{222}Rn) are presented as anomaly maps. In addition, the degassing values of all parameters (CO_2, H_2S, ^{222}Rn, ^{220}Rn, gamma radiation) have been plotted over a segment of the geological cross section C.

3.1 Determination of diffuse CO_2 emissions

The data set consists of 925 measurements ranging from non-detectable values up to a maximum CO_2 emission of 1,467.5 g/m^2/d. The map shows the interpreted results of CO_2 emissions (Fig. 5). Interpreted fault lineaments have been mapped based on the statistical separation of the peak population from lower values. This allows inferring the centers of the geothermal anomalies. Population PI represents the peak values and points to areas of strongest gas flux. The population of background values has not been considered and was therefore excluded from the map.

Degassing rates along discrete fault planes varied from non-detectable values up to peak population values. In particular at fault intersection points (I, II) or areas with a high fault density (III) increased rates have been observed. The map of plotted CO_2 data also illustrates that the degassing anomalies follow the bended fault lineaments that represent the Brady's fault step over zone (IV). Large areas to the West and East of the Brady's fault zone have been without detectable CO_2 emissions. Highest CO_2 flux occurred in the northern part of the study area and in particular within the step over (IV) of the Brady's fault zone, where a large number of small, NE-striking fault lineaments have been mapped. The plots of interpreted fault lineaments show the internal structure of the step over in detail and indicate areas with increased permeability. CO_2 degassing anomalies appeared predominantly as elongated distinct segments of NNE to NE orientation being displaced against each other (set of multiple left steps). Two small anomalies of CO_2 and H_2S emissions in the Southwest coincided with an abandoned acreage at the vegetable dehydration plant (V). The H_2S and CO_2 anomaly at the abandoned acreage might be explainable by the previous utilization of the acreage. The CO_2 anomaly (VI) to the North of the vegetable dehydration plant seems to be caused by variations of the natural boundary conditions (i.e., air temperature, atmospheric pressure) and was not considered for further interpretation (Jolie et al., 2014b).

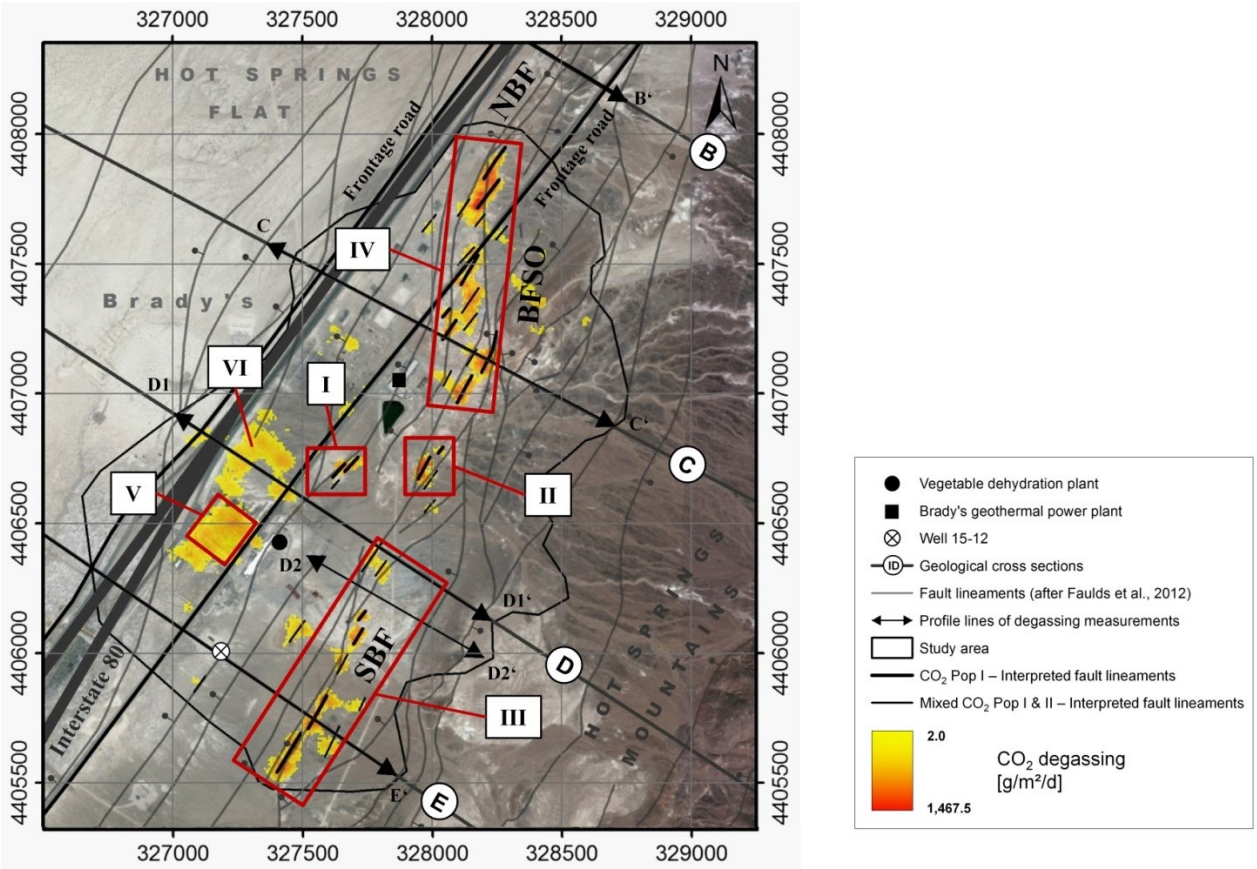

Figure 5: The map shows CO_2 emissions of the peak and mixed population from the Brady's geothermal system while values of the background population PII are masked (from Jolie et al., 2014b). CO_2 degassing anomalies marked by a red box and labeled by Roman numerals (I-VI) are explained in the text. SBF: Southern Brady's fault; NBF: Northern Brady's fault; BFSO: Brady's fault step over; Coordinate System: NAD 1983 UTM Zone 11N.

3.2 Determination of diffuse radon emissions

The data set consists of 476 radon measurements. Radon values (^{222}Rn) vary from 1,472.8 Bq/m³ up to 1,174,669 Bq/m³. Illustrated is the map with the interpreted results of radon emissions according to the statistical analysis of the probability plot (Fig. 6). The variation of radon decay products is strongly linked to the mapped fault pattern. Intensity of radiation varies along fault zones, which indicates different structural permeabilities along single fault planes. It is characteristic that the peak values of radon occur in particular at fault intersections (I), along dense arrangements of fault lineaments (II) and at the Brady's fault step over (III). The overall orientation of the anomalies is NNE to NE. Many of the anomalies are arranged along the broad Brady's fault zone. Highest radon activity occurs in the central part of the Brady's fault step over (III) where maximum CO_2 values have been measured as well. The shape of the anomaly suggests a set of connected clusters being slightly displaced against each other. In the western part of the study area (IV) large NE-oriented anomalies have been identified with increased radon emissions.

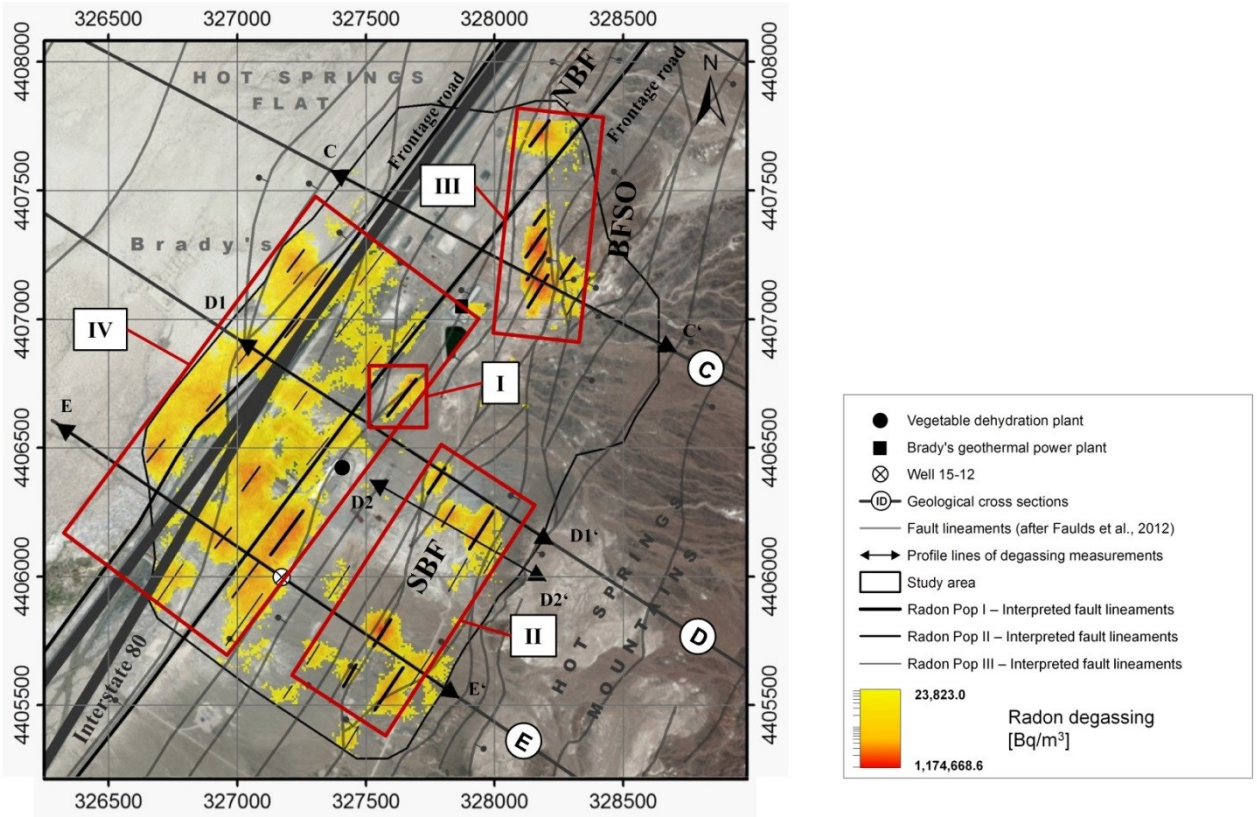

Figure 6: The map shows the radon emissions of population PI-PIII from the Brady's geothermal system while values of the background population PIV are masked (from Jolie et al., 2014b). Radon degassing anomalies marked by a red box and labeled by Roman numerals (I-IV) are explained in the text. SBF: Southern Brady's fault; NBF: Northern Brady's fault; BFSO: Brady's fault step over; Coordinate System: NAD 1983 UTM Zone 11N.

3.3 Profile C-C'

The Profile C-C' shows the exemplary variation of all monitored parameters (CO_2, H_2S, ^{222}Rn, ^{220}Rn, gamma radiation) along geological cross section C (Fig. 7). Describing the cross section for gamma radiation from west to east the first detectable peak (I) of 79.2 nSv/h was found at the Interstate I80, followed by a smaller peak (II) of 76.8 nSv/h at two open catchment basins within the area of geothermal production wells (between faults 7 and 8). The subsequent minimum (III) was measured at the frontage road (EF) east of the Interstate I80. Further to the east the curve shows three distinct and connected peak values (IV, V, VI) at the Brady's fault step over (faults 11, 12, 13), which range of 75.0-79.2 nSv/h. The following decrease (VII) occurs at a topographic high. East of the topographic high, gamma radiation increases again (VIII). Thoron describes a relatively smooth curve with a large depression (I) in the central part (fault 8), but without apparent peak values. East of the low a flattened peak (II) with values ranging from 6,647-6,833 Bq/m^3 has been determined that coincides partly with the Brady's fault step over fault. The radon curve starts with decreasing values (I) to the East. Between the Interstate I80 and the frontage road (EF) a broad plateau (II) with increased values up to 10,930 Bq/m^3 follows. At the Brady's fault step over peak values (III) with a maximum of up to 134,741 Bq/m^3 have been determined (faults 12, 13). At least five major faults (faults 11, 12, 13, 27, 28) are known in that area (Faulds et al., 2012; Jolie et al., 2012a, 2014a). East of the Brady's fault zone the curve returns to mean values (IV). CO_2 and H_2S profiles show a very similar pattern with different magnitudes. Across the Brady's fault step over two distinct peaks (CO_2: II, III; H_2S: I, II) become apparent for both parameters (faults 11, 13). The main peak of CO_2 has a very broad shape and lies across two major fault lineaments (faults 12, 13). At fault 29 an H_2S anomaly is indicated (III) even below the detection limit of the device, being congruent with a CO_2 anomaly (IV).

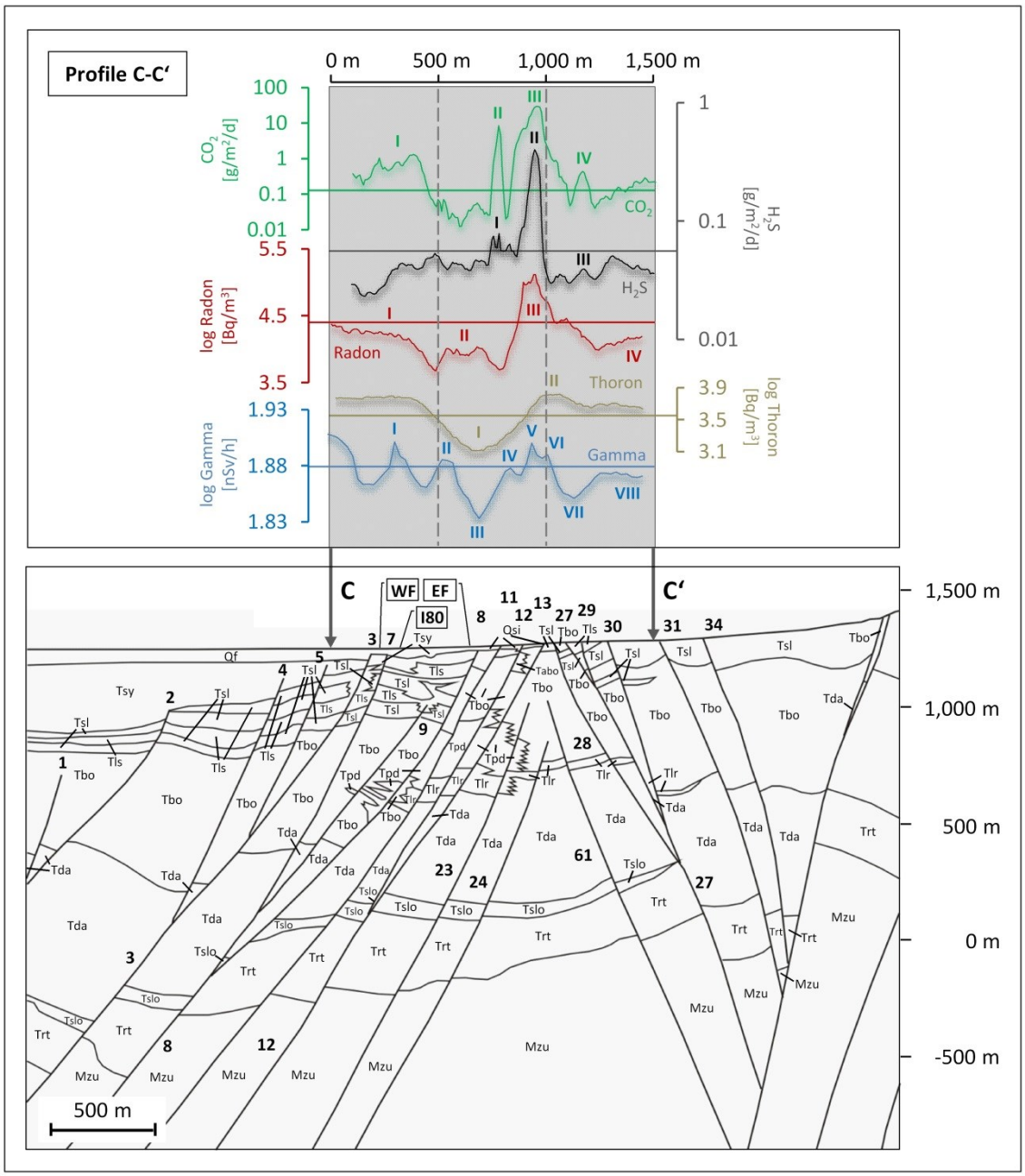

Figure 7: The diagram illustrates the variation of five monitored parameters (CO_2, H_2S, ^{222}Rn, ^{220}Rn, gamma radiation) along cross section C-C' (geological cross section from Faulds, unpublished data, 2011). Horizontal reference lines: CO_2 = 0.13 g/m²/d (detection limit); H_2S = 0.057 g/m²/d (detection limit); ^{222}Rn = log 4.41 (mean of all data); ^{220}Rn = log 3.56 (mean of population PIII); gamma radiation = log 1.88 (mean of all data). Color-coded Roman numerals along the data curves indicate anomalies and interpretation for each numeral can be found in the text. Arabic numerals are used for fault labeling. WF: Western frontage road; I80: Interstate I80; EF: Eastern frontage road.

4. CONCLUSION

In combination with the 3D structural-geological model (Jolie et al., 2012a, 2014a) conceptual models of the subsurface gas migration can be developed. Some of the deep fault zones are indicated as impermeable fluid recharge barriers, others seem to channel the geothermal fluids (Oppliger et al., 2005). The outline of active geothermal surface manifestations along the central Brady's fault conforms to the mapped faults and indicates structural permeability. From the developed 3D structural-geological model (Jolie et al., 2012a, 2014a) it is known that fault lineaments with increased degassing rates are very deep-rooting fault zones, which reach into the Mesozoic basement. Fault lineaments with minor gas emissions are often synthetic faults, which root into main faults. Several other faults also reach into the Mesozoic basement without indicating increased gas emissions, which might be related due to their orientation (strike and dip), their dimensions, the fact that they often die out laterally within the 3D model and their distance to the main geothermal manifestations. Based on the results of degassing surveys it is possible to delineate the orientation of permeable fault lineaments. The combined approach of 3D geological modeling and diffuse degassing measurements is a useful method in early stage geothermal exploration to describe and quantify structural permeability of a geothermal system. It is now of great interest to better understand how exactly degassing anomalies extend from the origin of the gas at depth to the surface in order to infer preferential pathways for fluid migration.

REFERENCES

Bourdon, B., Turner, S., Henderson, G.M., Lundstrom, C.C., 2003. Introduction to U-series geochemistry. Reviews in mineralogy and geochemistry, 52(1), 1-21.

Cardellini, C., Chiodini, G., Frondini, F., Granieri, D., Lewicki, J., Peruzzi, L., 2003. Accumulation chamber measurements of methane fluxes: application to volcanic-geothermal areas and landfills. Applied geochemistry, 18(1), 45-54.

Chiodini, G., Caliro, S., Cardellini, C., Granieri, D., Avino, R., Baldini, A., Donnini, M., Minopoli, C., 2010. Long-term variations of the Campi Flegrei, Italy, volcanic system as revealed by the monitoring of hydrothermal activity. Journal of Geophysical Research: Solid Earth (1978-2012), 115(B3).

Faulds, J.E. and Garside, L.J., 2003. Preliminary geologic map of the Desert Peak – Brady geothermal fields, Churchill County, Nevada. Nevada Bureau of Mines and Geology, Open-File Report, 03-27.

Faulds, J.E., Ramelli, A.R., Garside, L.J., Coolbaugh, M.F., Green, H.L., 2012. Preliminary geologic map of the Desert Peak Quadrangle, Churchill County, Nevada (scale 1:24,000). Nevada Bureau of Mines and Geology, Open-File Report, 12-5.

Fridriksson, T., Kristjánsson, B.R., Ármannsson, H., Margrétardóttir, E., Ólafsdóttir, S., Chiodini, G., 2006. CO_2 emissions and heat flow through soil, fumaroles, and steam heated mud pools at the Reykjanes geothermal area, SW Iceland. Applied Geochemistry, 21(9), 1,551-1,569.

Giammanco, S., Gurrieri, S., Valenza, M., 1998. Anomalous soil CO2 degassing in relation to faults and eruptive fissures on Mount Etna (Sicily, Italy). Bulletin of Volcanology, 60(4), 252-259.

Hernández, P.A., Notsu, K., Salazar, J.M., Mori, T., Natale, G., Okada, H., Virgili, G., Shimoike, Y., Sato, M., Pérez, N.M., 2001. Carbon dioxide degassing by advective flow from Usu volcano, Japan. Science, 292(5514), 83-86.

Jolie, E., Faulds, J., Moeck, I., 2012a. The development of a 3D structural-geological model as part of the geothermal exploration strategy – a case study from the Brady's geothermal system, Nevada, USA. Stanford Geothermal Workshop Proceedings, 37, SGP-TR-194.

Jolie, E., Klinkmueller, M., Moeck, I., 2012b. Diffuse degassing measurements as a geochemical exploration tool: A case study from the Brady's geothermal system (Nevada, USA). Geothermal Resources Council Transactions, 36, 685-688.

Jolie, E., Klinkmueller, M., Moeck, I., 2014a. Quantitative structural-geological exploration of fault-controlled geothermal systems – A case study from the Basin-and-Range Province, Nevada (USA). Geothermics, doi: 10.1016/j.geothermics.2014.10.003.

Jolie, E., Klinkmueller, M., Moeck, I., 2014b: Diffuse surface emanations as indicator of structural permeability in fault-controlled geothermal systems. Journal of Volcanology and Geothermal Research, doi: 10.1016/j.jvolgeores.2014.11.003.

Oppliger, G., Coolbaugh, M., Shevenell, L., Taranik, J., 2005. Elucidating Deep Reservoir Geometry and Lateral Outflow through 3-D Elastostatic Modeling of Satellite Radar (InSAR) Observed Surface Deformations: An Example from the Bradys Geothermal Field. Geothermal Resources Council Transactions, 29, 419-424.

Padrón, E., López, D.L., Magaña, M.I., Marrero, R., Pérez, N.M., 2003. Diffuse degassing and relation to structural flow paths at Ahuachapan Geothermal Field, El Salvador, Geothermal Resources Council Transactions, 27, 325-330.

Parkinson, K.J., 1981. An improved method for measuring soil respiration in the field. Journal of Applied Ecology, 18, 221-228.

Pérez, N.M., Salazar, J.M.L., Hernández, P.A., Soriano, T., López, D.L., Notsu, K., 2004. Diffuse CO_2 and ^{222}Rn degassing from San Salvador volcano, El Salvador, Central America, in: Rose, W.I., Bommer, J.J., López, D.L., Carr, M.J., Major, J.J. (Eds.), Natural Hazards in El Salvador, Geological Society of America, Special Papers, 375, pp. 227-236.

West Systems, 2002. Carbon dioxide flux meter, Handbook, Release 4.11, August 2002, URL: http://www.westsystems.com/documentation/SoilFluxPortable0503.pdf (Retrieved January 17th, 2014).